

# 3D Printed Optics Achieves Broadband Structured Light

Leerin Perumal, Stefan Hengsbach, Moslem Mahdaviifar, Jan Korvink, and Andrew Forbes\*

Structured light has gained in popularity of late, fueled by a toolbox for arbitrary control of light's many degrees of freedom. Although this toolbox is very sophisticated and diverse, it is still primarily centered on single wavelength digitally controlled structured light, only recently expanding into broadband structured light modes. Here, tools are combined from Fourier optics with recent advances in grayscale 3D nano-printing of optical materials to design and fabricate micro-optical elements for the creation of broadband structured light beams by phase-only and full complex amplitude modulation. Importantly, this approach allows to fabricate a single device at a design wavelength and later use it for non-design wavelength operation, as well as multiple wavelengths simultaneously, which is demonstrated across  $\approx 200$  nm bandwidth. A myriad of optics is created to produce orbital angular momentum, Hermite–Gaussian, and Laguerre–Gaussian beams, with measured purities in the 94% – 100% range, for non-design wavelengths. This work provides a compact, simple and cost-efficient tool for control of the spatial-spectrum of structured light.

relationship with structured matter<sup>[9,10]</sup> and light-matter interactions, e.g., with liquid-crystals,<sup>[11]</sup> for structuring materials,<sup>[12]</sup> at structured matter boundaries for generalized laws of reflection and refraction<sup>[13]</sup> and in control of matter.<sup>[14]</sup> This trend has led to the emerging field of flat-optics for the creation and control of structured light<sup>[15]</sup> by arrays of artificial atoms, e.g., metasurfaces,<sup>[16–19]</sup> away from the traditional route of digitally based solutions, e.g., with spatial light modulators<sup>[20]</sup> and digital micro-mirror devices.<sup>[21,22]</sup>

In particular, in a drive to exploit many of light's DoFs simultaneously, the need for solutions that are broadband has arisen. Approaches to circumvent wavelength dependence have seen general dispersion control at the nanoscale emerge as a modern tool,<sup>[23]</sup> with demonstrations of broadband imaging<sup>[24,25]</sup> and detection,<sup>[26]</sup> even with metasurface assisted fibers,<sup>[27]</sup>

and with spherulite crystals.<sup>[28,29]</sup> In the context of structured light, advances include orbital angular momentum (OAM) control at visible wavelengths on-chip<sup>[27]</sup> and using catenary principles at the nanoscale.<sup>[30]</sup> Wavelength dependence can also be exploited for multi-functional elements, e.g., focussing<sup>[31]</sup> and OAM<sup>[32]</sup> that is color dependent. In 3D printed micro-optics with nanoscale resolution, the structure of matter can act as a spectral filter, e.g., by dyes<sup>[33]</sup> and spectrally selective micro-pillars,<sup>[34,35]</sup> thus ensuring functionality across pre-designed wavelengths.

Here we combine complex amplitude modulation with modern nanoscale 3D printers of optics to design and fabricate micro-optical elements for high fidelity structured light that operates far from the design wavelength, including broadband, as illustrated in **Figure 1a**. We print both 2-level binary and 256-level grayscale phase elements that can simultaneously act on both the amplitude and phase of the incoming light, and unpack the steps to go from a desired amplitude and phase in the structured light to a wavelength invariant 3D printed optic. We validate the approach by creating various structured light patterns experimentally using multiple wavelengths beyond the design wavelength, all with high fidelity. The penalty is only a negligible decrease in efficiency. This work marries the traditional approaches of computer generated holograms for structured light with modern trends in fast, inexpensive, and accurate 3D printed optics, opening a new route to compact solutions of structured light.

## 1. Introduction

In the past few decades the concept of tailoring light's many degrees of freedom (DoFs) to craft unique optical fields, commonly referred to as structured light,<sup>[1]</sup> has gained in popularity. Since its inception, structured light has sparked a revolution through its ability to tailor light for purpose across diverse sectors,<sup>[2,3]</sup> including high-power applications,<sup>[4]</sup> quantum optics<sup>[5]</sup> and nonlinear optics,<sup>[6]</sup> with control directly from lasers<sup>[7]</sup> and beyond the spatial DoFs to temporal control.<sup>[8]</sup> An important branch of structured light is its symbiotic

L. Perumal, M. Mahdaviifar, A. Forbes  
School of Physics  
University of the Witwatersrand  
Johannesburg 2050, South Africa  
E-mail: [andrew.forbes@wits.ac.za](mailto:andrew.forbes@wits.ac.za)

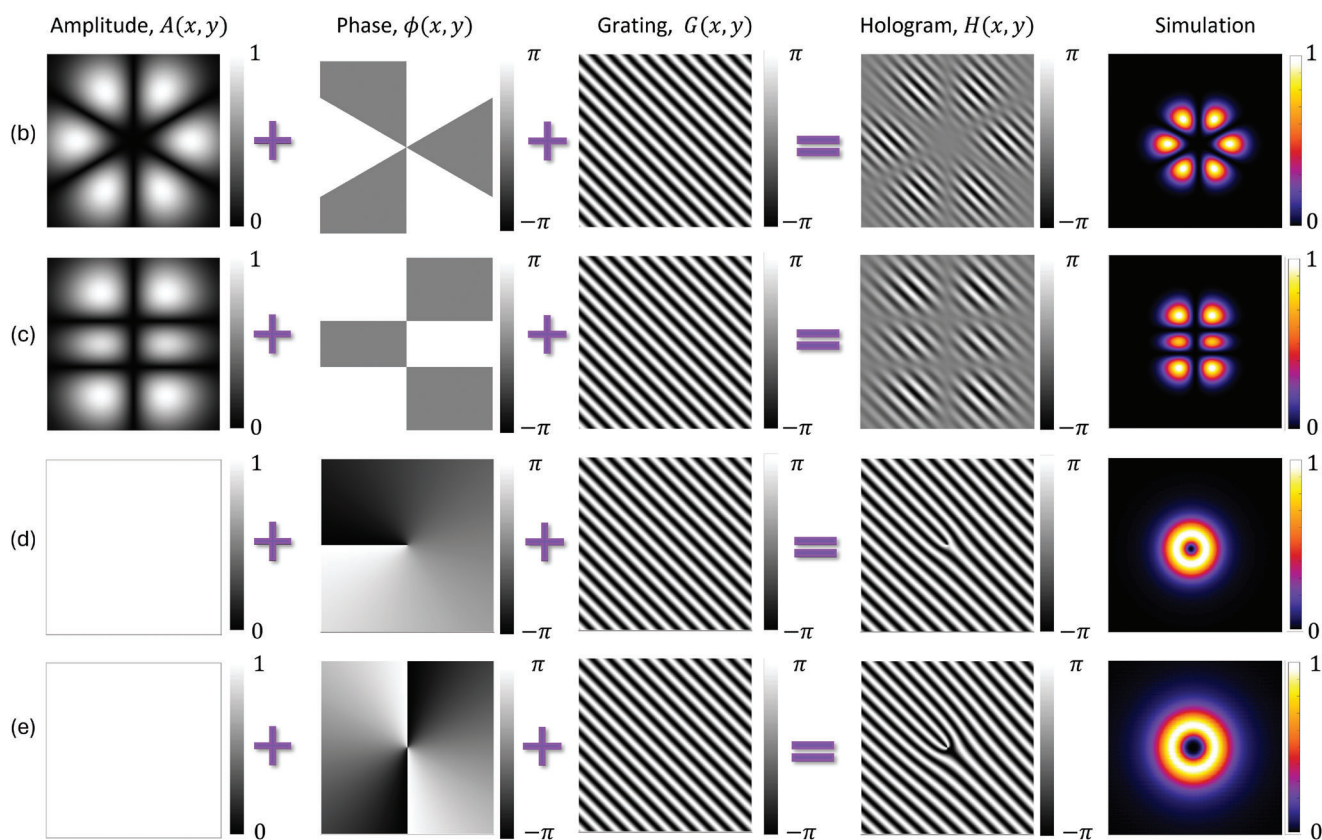
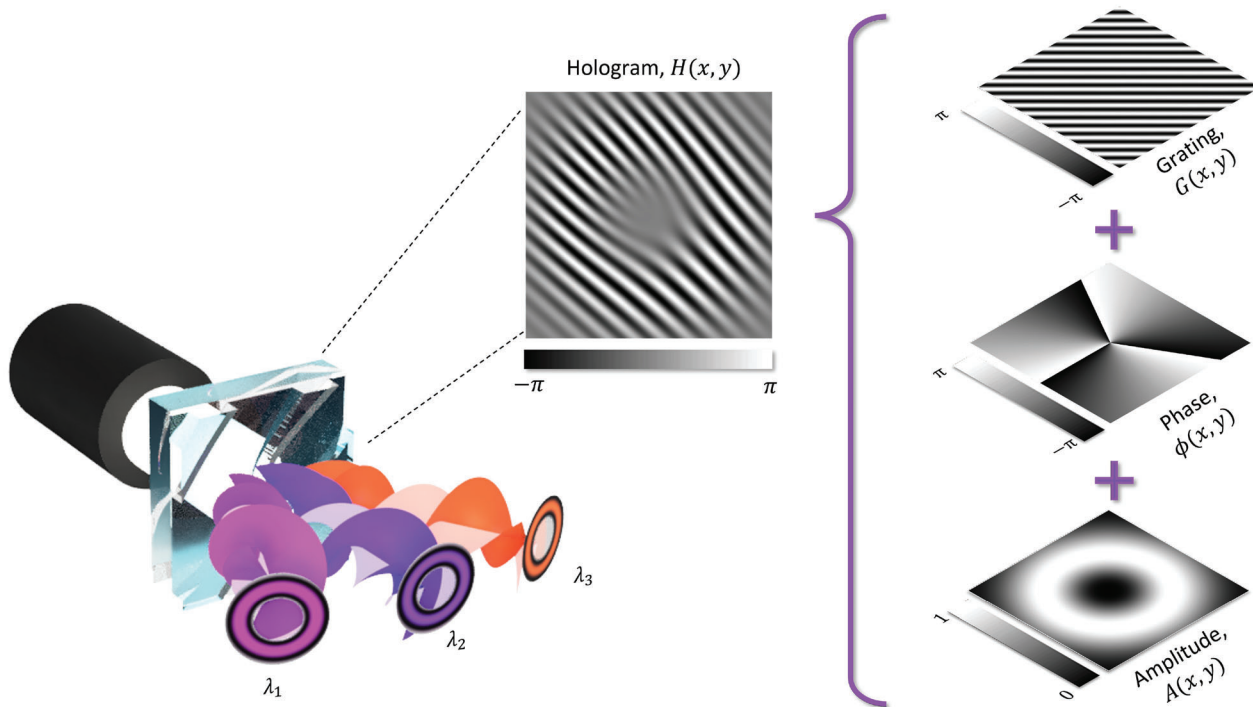
S. Hengsbach, J. Korvink  
Institute of Microstructure Technology  
Karlsruhe Institute of Technology  
76344 Eggenstein-Leopoldshafen, Germany

 The ORCID identification number(s) for the author(s) of this article can be found under <https://doi.org/10.1002/adom.202403028>

© 2025 The Author(s). Advanced Optical Materials published by Wiley-VCH GmbH. This is an open access article under the terms of the [Creative Commons Attribution](#) License, which permits use, distribution and reproduction in any medium, provided the original work is properly cited.

DOI: 10.1002/adom.202403028

(a)



## 2. Design and Fabrication of Optics

### 2.1. Hologram Generation

Assume we have some incident light field  $U_{\text{in}}(x, y) = A_{\text{in}}(x, y) \exp(i\phi_{\text{in}}(x, y))$  and desire an output field,  $U_{\text{out}}(x, y) = A_{\text{out}}(x, y) \exp(i\phi_{\text{out}}(x, y))$ , requiring complex amplitude modulation (both amplitude and phase modulation) of the incident field by a transmission function,  $T(x, y) = U_{\text{out}}/U_{\text{in}} = A(x, y) \exp(i\phi(x, y))$ . It is assumed that the fields are normalized so that energy conservation is not violated, effectively implying that the output field is “cookie cut” from the input. In general we need to manipulate both the phase and amplitude of the incident beam, i.e., complex amplitude modulation, but to keep our 3D printed optics as simple as possible we will restrict the solution to a phase-only implementation but still with the full complex amplitude modulation functionality, i.e.,  $T(x, y) = A(x, y) \exp(i\phi(x, y)) \equiv \exp(iH(x, y))$ . We further assume we have specified all the phases for a specific wavelength,  $\lambda_0$ . There are many approaches from computer generated holograms to find the desired function,  $H(x, y)$ . For instance, since we can only remove (and not create) light when the amplitude is modulated, this undesired light must either go to lower diffraction orders or higher diffraction orders. This will reduce the efficiency of the shaping element by an amount that depends on the spatial structure of the input and the output. Pushing light to higher diffraction orders results in

$$H(x, y) = f(A) \sin(\phi(x, y)) \quad (1)$$

where  $f(A) = J_1^{-1}[A(x, y)]$  is the inverse first-order Bessel function.<sup>[36]</sup> While this formulation and our results to follow can be extrapolated to any structured light form, in the remainder of this work we will consider as the desired amplitude and phase that of the Hermite–Gaussian (HG) and Laguerre–Gaussian (LG) mode sets, given by

$$\text{HG}_m^n(x, y) = \sqrt{I_0} H_n\left(\frac{\sqrt{2}x}{w_0}\right) H_m\left(\frac{\sqrt{2}y}{w_0}\right) \times \exp\left(-\frac{x^2 + y^2}{w_0^2}\right) \quad (2)$$

where  $n$  and  $m$  are mode indices,  $w_0$  is the embedded Gaussian beam size at  $z = 0$  and  $I_0$  is found by normalizing the energy to  $E$ , to return

$$I_0 = 2\mu_0 c \frac{E}{\pi w_0^2 n! m! 2^{m+n-1}} \quad (3)$$

with  $\mu_0$  and  $c$  the vacuum permeability and speed of light, respectively. We can change to the Laguerre–Gaussian basis

$$\text{LG}_\ell^p(r, \theta) = \sqrt{I_0} L_p^\ell\left(\frac{2r^2}{w_0^2}\right) \left(\frac{\sqrt{2}r}{w_0}\right)^{|\ell|} \times \exp\left(-\frac{r^2}{w_0^2}\right) \exp(-i\ell\theta) \quad (4)$$

where  $\theta$  is the azimuthal angle, and  $p$  and  $\ell$  are mode indices and

$$I_0 = 2\mu_0 c \frac{2E p!}{\pi w_0^2 (p + |\ell|)!} \quad (5)$$

These two examples are pertinent since they encompass both cartesian and cylindrical symmetries, while  $\ell \neq 0$  imparts orbital angular momentum (OAM) to the light,<sup>[37]</sup> a topic of considerable interest in the community.

Now we invoke a known Fourier trait: linear phase ramps do not change their pitch if modulated by an amount differing from  $2\pi$  - gratings remain gratings if operated at a new wavelength, but they now produce new diffraction orders. Since any complex function can be written as a suitably sampled linear phase grating, i.e.,  $|f(x)| \exp(i\psi) = |f(x)| \exp(i\psi x/x_0) \delta(x - x_0)$ , the same will be true for arbitrary transmission functions.<sup>[38]</sup> With this in mind, suppose that a linear phase ramp of the form  $\exp(i2\pi x/d_x + i2\pi y/d_y) \equiv \exp(iG(x, y))$  is added to the desired phase, with periods of  $d_x$  and  $d_y$  in the  $x$  and  $y$  directions, respectively. Our new hologram becomes

$$H(x, y) = f(A) \sin(\phi(x, y) + G(x, y)) \quad (6)$$

To see the effect of operating at a wavelength,  $\lambda$ , instead of  $\lambda_0$ , we can expand our desired transmission function as a Fourier series using the harmonic function  $\phi(x, y) + G(x, y)$ , giving rise to

$$T(x, y) = \sum_m \eta_m(\lambda) A(x, y) \exp(im(\phi(x, y) + G(x, y))) \quad (7)$$

where

$$\eta_m(\lambda) = \text{sinc}\left(\pi\left(m - \frac{\lambda}{\lambda_0}\right)\right) \quad (8)$$

In the first diffraction order,  $m = 1$ , we have

$$T(x, y) = \text{sinc}(\pi\Delta\lambda/\lambda_0) \exp(iG(x, y))$$

**Figure 1.** a) 3D printed optics can be used to modulate multiple wavelengths ( $\lambda_1, \lambda_2, \lambda_3$ ) of structured light, either discretely or simultaneously. We outline how to translate computer generated holograms (inset) for structured light as the basis for the design of broadband diffractive optics printed by grayscale lithography. The concept is illustrated here for multi-colored orbital angular momentum light. The inset is the hologram generation process for the example of LG modes of  $\text{LG}_3^0$ , created through complex amplitude modulation. The hologram has the combined functions of a grating, a phase and an amplitude. The final grayscale hologram is a phase-only mask (but with all the aforementioned traits) comprised of 256 grayscale levels that map to a discrete phase shift,  $\phi \in [-\pi, \pi]$ . The hologram generation process for other modes including the superposition of LG modes ( $\text{LG}_3^0 + \text{LG}_{-3}^0$ ) (b), HG ( $\text{HG}_1^2$ ) (c) as well as the pure modes of  $\text{LG}_1^0$  (d) and  $\text{LG}_2^0$  (e), respectively. Elements of the last column from (b) to (e) are related to the simulation of mentioned modes.

$$\underbrace{\times A(x, \gamma) \exp(i\phi(x, \gamma))}_{\text{desired beam}} \quad (9)$$

Ignoring the grating term (which sets the direction of the light), we see that we have the desired beam with an efficiency given by the sinc function. Note that this efficiency drop is determined by the factor  $\Delta\lambda/\lambda_0$ , the fractional change of the wavelength, i.e., a 10% change in wavelength has the same effect regardless of the actual wavelength. To give a quantitative feel for this, if  $\lambda_0 \approx 550$  nm and  $\Delta\lambda \approx \pm 150$  nm (the entire visible spectrum), then the maximum drop in efficiency is about 10%, while a similar analysis for the entire telecom band reveals a maximum efficiency drop of less than 1%. Despite this slight drop in efficiency, the *function* of the element is predicted to create the same structured light pattern regardless of wavelength. It is in this sense that we refer to the design as broadband and wavelength independent. Since the functional form is the same, the purity and fidelity of the produced field are predicted to be independent of wavelength too. The final hologram can thus be conceptualized as the sum of a linear phase ramp (grating), the desired phase, and the desired amplitude, shown in the inset of Figure 1a for the example of an LG mode carrying orbital angular momentum (LG<sub>3</sub><sup>0</sup>). Holograms can produce structured light modes through manipulation of both the phase and amplitude (complex-amplitude) or phase-only modulation. In Figure 1b,c, we illustrate how complex-amplitude holograms are generated to produce a superposition of LG modes (LG<sub>3</sub><sup>0</sup> + LG<sub>-3</sub><sup>0</sup>) as well as HG (HG<sub>1</sub><sup>2</sup>), respectively. In this case the hologram is the sum of a grating, an amplitude and a phase mask. With respect to phase-only holograms, the amplitude mask is omitted and the hologram is the sum of the phase mask and grating alone. This is illustrated in (d) and (e) parts of Figure 1 for holograms that create OAM modes with azimuthal indices  $l = 1$  and  $l = 2$ , respectively.

## 2.2. Grayscale Lithography Combined with 2 Photon Polymerization

Grayscale lithography<sup>[39]</sup> forms smooth variations in surface topography by varying the intensity of the light used to crosslink a monomer solution. In contrast, two-photon polymerization (2PP)<sup>[40,41]</sup> is based on the confinement of photon-driven energy absorption by a monomer to a small sub-volume of a strongly focused light beam. Two photons must be co-localised to overcome the available energy gap, which in turn overcomes the Abbé limit. The combination of these two techniques allows maintaining the surface roughness in the 10 nm - 25 nm range, also along curved surfaces.

In combination, these two techniques overcome many of the limitations of typical 3D-printing methods, in which a CAD-model is usually converted into cubic materialized voxels from planar slices of the model, the slices taken along a third orthogonal direction.<sup>[42]</sup> Once printed, such layers are typically visible as steps in the final geometry. To increase the surface quality, the slicing distance normally has to be reduced, resulting in larger discretization sets.

Typical printing methods based on fused deposition modeling (FDM) which extrudes fused polymers through a fine nozzle can

reach resolutions down to 200 μm. Higher resolutions can be achieved with stereolithography (SLA) based printing methods which use UV-light in combination with photochemically active components (resin) to harden the resin locally by a digital mask. With this method resolutions down to 100 μm can be reached. 2PP printers can reduce this to ≈50 nm or smaller<sup>[43]</sup> by using a tight focusing objective in combination with a femtosecond (fs) pulse width laser, and a photosensitive liquid as the photoresist. Polymerization then initiates at the center of the focal spot, since only at this point the energy density is high enough for a photochemical reaction.

Polymerization only occurs at the center of the focus spot since only at this point the density of energy is high enough to lead to a photochemical reaction. This interaction zone is called a voxel, a “volumetric pixel.” However, even if the shape of the structure can be adapted better by 2PP printing, layers are still visible due to the discretization into Cuboid-like voxels. This can be improved by making a use of the linear behaviour of the laser power and the voxel size. The laser power can be adapted while printing, so that the voxel size corresponds to the desired shape of the structure. To achieve a perfect match, the system used for printing needs to be calibrated to determine the laser power required for a particular voxel height. For the fabrication of the optical structures, a QuantumX (Nanoscribe GmbH) had been used. To upload files to the printer, stereolithography (STL) files or in the case of grayscale lithography, grayscale images (up to 1024 Bit) are suitable. The input files are converted by the software “GrayscaleX” (Nanoscribe GmbH) into machine-readable data.

To print the computer-generated hologram (CGH), a visual representation of a matrix of calculated relative phase shifts,  $\phi \in [-\pi, \pi]$  has been mapped to grayscale values from 0 to 255, for a 256-level approximation to the smooth surface. For illustration, assume that in a very small localized region (purple) in Figure 2a that there are three discrete phase shifts needed, represented by three grayscale values. When uploaded to the calibrated printer, these grayscale values are mapped to a discrete height in the  $z$  direction, varying in 256 steps from 0 to  $d_{\text{max}}$ . If the same grayscale hologram is converted to a 2-level binary approximation, as seen in Figure 2b, then the hologram will only be able to impart a 0 (gray) or  $\pi$  (white) phase shift. A 256-level hologram has a theoretical maximum efficiency of ≈100%, while a 2-level hologram has a theoretical maximum efficiency of ≈42%. One can thus immediately appreciate the benefit of grayscale lithography. Henceforth, for conciseness, we will refer to the 256-level approach as “grayscale” and the 2-level approach as “binary”. In this way, a 2D hologram is converted into a 3D model and a designed template of the desired diffractive optical element.

## 2.3. Fabrication Process

The fabrication process of the hologram, as illustrated in Figure 3, was performed in the following main steps. Initially, the computer generated holograms (a) had to be converted (b) into machine readable format (c). Next, the hologram was permanently written onto the resist. For this, the sample was prepared (d, e), printed (f), and developed (g).

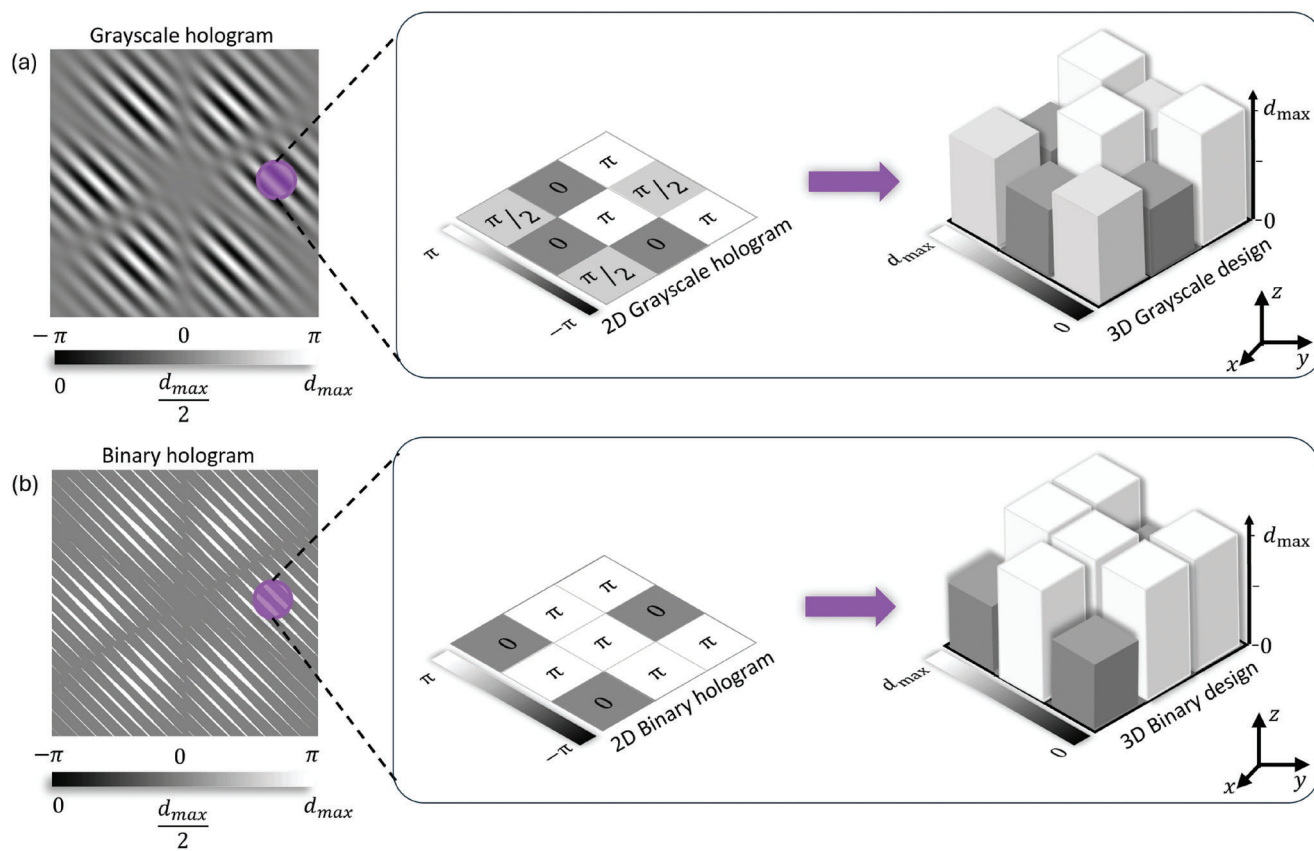


**Figure 2.** a) The final grayscale hologram is a phase-only mask comprised of 256 grayscale levels that map to a discrete phase shift between  $-\pi$  and  $\pi$ . For example, consider a localized region (purple) with only 3 of the 256 steps:  $\phi = 0 \rightarrow$  dark gray (graylevel = 128),  $\phi = \pi/2 \rightarrow$  light gray (graylevel = 192) and  $\phi = \pi \rightarrow$  white (graylevel = 255). When uploaded to a calibrated printer, these grayscale values are mapped to discrete heights/thickness in the  $z$  direction, from 0 to  $d_{\max}$  in 256 steps (only three steps shown for illustrative purposes). In this way, a 2D grayscale hologram is converted into a 3D model and a designed template of the desired optic. b) If the same grayscale hologram is converted to a 2-level binary approximation, then the hologram will only be able to impart a 0 (gray) or  $\pi$  (white) phase shift with corresponding heights of  $d_{\max}/2$  and  $d_{\max}$ , respectively.

### 2.3.1. Hologram Upload

When a beam of light is incident on the desired optical element it should experience a relative phase shift at each spatial position which can be described by a continuous phase function. The corresponding height,  $d(x, y)$ , to impart the desired phase, is given by

$$d(x, y) = \frac{\lambda_0 H(x, y)}{2\pi(n_i - n_0)} \quad (10)$$

where  $n_i$  is the refractive index of the printing material (the resin), and  $n_0$  is the refractive index of the surrounding material, which in our case (and often true) is air,  $n_0 = 1$ . Because of the cyclic nature of phase functions, the physical optic need never exceed a height of  $d_{\max} = \frac{\lambda_0}{n-1}$ , but can be some integer multiple of this for the same efficiency (but with the danger of more losses due to absorption or scattering). This height is one of the crucial parameters that must be set as the maximum printed height in the printing process,  $d_{\max}$ . Once a full 3D structure has been realized, GrayScribeX can be used to segment the model, either through manual or automated actions, to assist the printing process.

Depending on the objective lens used in the printer, the laser beam has a maximum area that it is able to print within, i.e., a field of view (FOV) at a given instance. If the desired structure is larger than this FOV, the model will be partitioned into printable segments that are equal in size to the FOV. Hence, when the model is printed it will be composed of many printed areas that appear to be “stitched” together. Depending on the size of the designed structure and the objective lens used, the discontinuity between each adjacent printed area, i.e., the stitching lines, may be noticeable and have a significant effect on the structure.

The structure is then further subdivided in the  $x$  and  $y$  planes (“hatched”), and subdivided in the  $z$  plane (“sliced”). Together the hatching and slicing distances dictate the volume of the resin that is polymerized for a given laser power, i.e., the voxel, which is typically thought of as the volumetric pixel in 3D printing.

### 2.3.2. Sample Preparation

The structures were printed on a fused silica microscope slide with a thickness of 700  $\mu\text{m}$ . The samples were cleaned by rinsing them with isopropanol and dried with  $N_2$  gas, and then placed for 5 min on a hotplate at 110  $^\circ\text{C}$ , illustrated in Figure 3d.

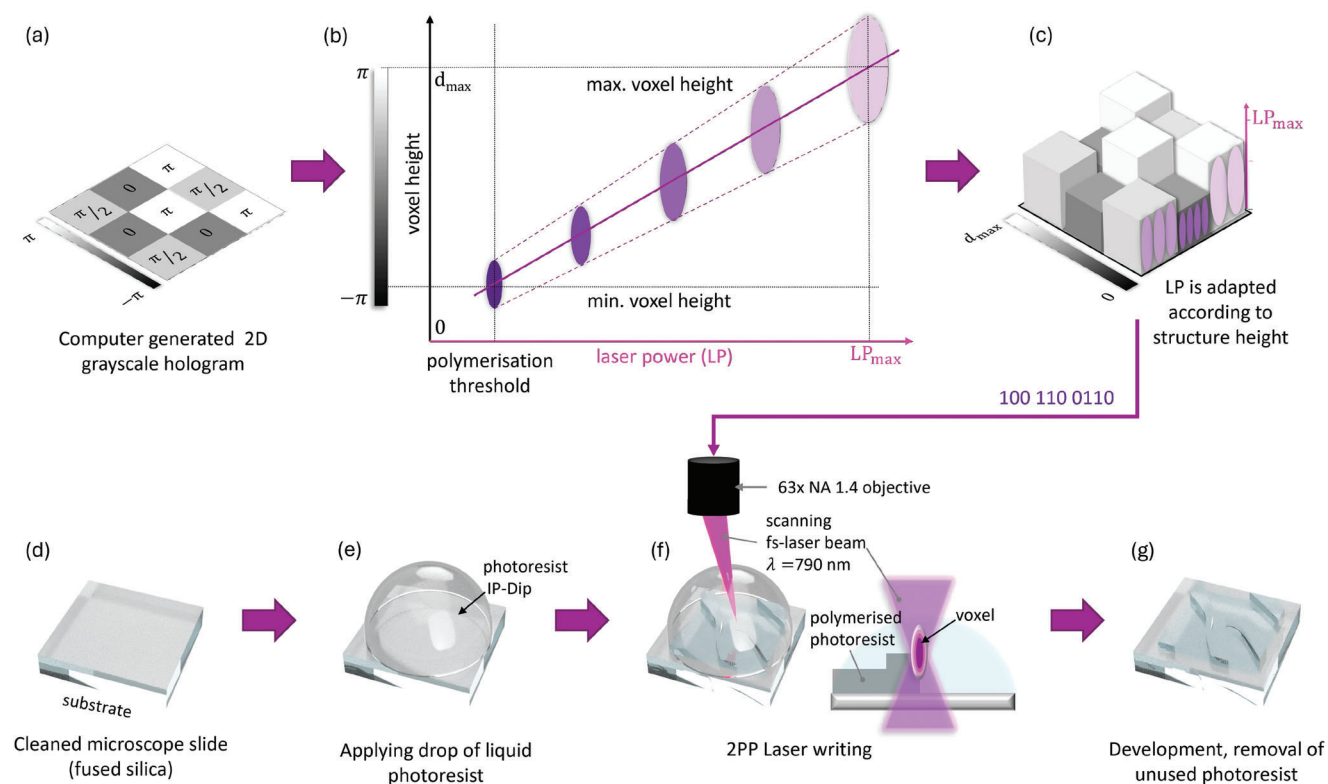


**Figure 3.** 3D-Printing process of a computer generated hologram. a) Before a hologram can be printed it has to be converted into machine readable data. To impart the desired phase, the height of the hologram is given by Equation (10). b) The linear dependence of the laser power (LP) on the print height (voxel height) is used to achieve the calculated height of the structures. A minimum power level is needed to polymerize a specific volume of photoresist. From this threshold on, there is a linear increase of the voxel size with the laser power until a maximum volume is reached. c) The laser power is thus adapted to the desired structure height and sent to the printer as data. d) The fabrication process starts with a microscope slide substrate cleaned with isopropanol. e) After drying and dehydration of the substrate, a liquid drop of photoresist is placed at the desired position. For the 2PP-Writing process, a microscope objective is dipped in the liquid photoresist so as to avoid diffraction effects that would occur at the glass-air interface. f) According to the 2PP principle, the resist polymerizes locally at the focus point of the laser beam following the pattern of (a). g) After printing, the unused excess photoresist is washed away using a mild solvent (PGMEA – propylene glycol methyl ether acetate), followed by a cleaning step with isopropanol.

Afterwards, a drop of liquid photoresist, IP-Dip (Nanoscribe GmbH) was placed on the substrate and mounted to a sample holder, as seen in Figure 3e.

### 2.3.3. Printing

We used the Quantum-X, housing a femtosecond pulsed laser (wavelength  $\lambda = 790$  nm), for printing via 2PP, as depicted in Figure 3f. The smallest volume of resin that can be polymerized for a given LP is the voxel, as seen in Figure 3b. Strong focussing using an objective in conjunction with a high photon density increased the probability of two photons being in the same place at the same time. This local increase in energy is sufficient for a photochemical reaction, resulting in polymerization of the photoresist. Since the energy distribution of the laser beam in the lens also follows a Gaussian distribution, the probability of a 2PP reaction out of the center is also highest here. At the edges of the Gaussian beam profile, the number of photons is no longer sufficient for a reaction. For this reason, the resulting voxel is smaller than the width of the laser beam, which makes it perfect suitable for optical applications. To create the desired design, the LP and

thus the voxel size is changed to achieve printed structures of varying height and width. If the height of the desired structure is greater than the structure that can be printed with the maximum voxel size, multiple layers are needed.

To print the optics, we opted for a 63× (NA 1.4) objective lens, optimized for the photoresist IP-Dip with a refractive index of  $n = 1.521$  (at  $\lambda = 589$  nm). This resulted in a structure height of 25  $\mu\text{m}$ , with the field of view limited to 150–200  $\mu\text{m}$ . The optic was designed to be 1500  $\mu\text{m} \times 1500 \mu\text{m}$  was thus segmented into 10  $\times$  10 printable areas. Other parameters such as the hatching and slicing distances, printing speed and laser power were

**Table 1.** Experimental modal purities.

Wavelength	OAM ( $l = 1$ )	Superposition ( $l = \pm 3$ )
457 nm	97%	95%
488 nm	96%	94%
514 nm	100%	97%
633 nm	100%	96%

then set and are summarized in Table 2. The printing lasted for approximately 26 h, about an hour per optic.

#### 2.3.4. Development

When printing, only a portion of the resin is polymerized in a particular region of interest, while the rest of the resin is left unused. In this way the printer is able to “carve” out the desired structure from the resin. Hence, to fully expose the printed structure one must remove all excess resin present on the substrate. This process is referred to as “development” and is done by submerging the sample in a propylene glycol methyl ether acetate (PGMEA) solvent for approximately 10 min. The solvent reacts with and dissolves the remaining un-polymerized resin while leaving the polymerized resin unaffected, thus exposing the printed structure as seen in Figure 3g. If the sample is removed too soon from the solvent, it is likely that all excess resin will not be adequately removed and the printed structure will not be properly exposed and, therefore, appear misshaped or warped. However, if the sample is left in the PGMEA solution for extended periods of time the solvent could weaken the polymer structure and thus compromise the quality and distort the shape of printed structure. Further cleaning of the substrate surface of other impurities, such as dust or fingerprints, is done by submerging the substrate with solvents such as isopropanol for an additional 5–10 min. The sample is then partially dried using a gentle stream of nitrogen gas, and left to completely dry out in a fumehood for 5 min.

### 3. Results

#### 3.1. Material Characterization

In what follows we will use the grayscale and binary LG mode ( $l = 1$ ) optics as typical examples of the optical quality produced.

**Length ( $x$ ) and width ( $y$ ).** Using a scanning electron microscope (SEM) and microscope the printed optics’ dimensions were measured to be  $\approx 1500 \mu\text{m}$  in both the  $x$ - and  $y$ -directions, as shown in Figure 4a,b. Hence, the optic’s size exactly matches that of the design hologram which was set to have a length and width of  $1500 \mu\text{m}$  in both the  $x$ - and  $y$ - directions.

**Spacing between structures.** When generating the hologram, a grating was encoded with a frequency  $g_x = 12000$  lines/m, and  $g_y = 12000$  lines/m for the grayscale holograms. This corresponds to a grating period,  $d = 83 \mu\text{m}$  in both the  $x$ - and  $y$ - directions. For the binary holograms  $g_x = 8000$  lines/m, and  $g_y = 8000$  lines/m. This corresponds to a grating period,  $d = 125 \mu\text{m}$  in both the  $x$ - and  $y$ - directions, as seen in the insets of Figure 4b.

**Surface roughness.** To analyze the surface and determine the printing resolution of the same vortex ( $l = 1$ ) optic, we examined it using a SEM as seen in Figures 4c. The smoothness of an optical surface is important because rough surfaces cause light to scatter and may lead to noise and/or cause aberrations to the generated mode. One expected distortion to the optics is the points where the various printed areas are “stitched” together. If we consider Figure 4c, we see a region of interest on the optic where the stitching lines are apparent (purple arrow). When measured, the stitching lines were  $\approx 8$  nm thick. Hence, depending on the size and

complexity of the designed optic this may be considered a negligible defect to the surface with minimal effect to the quality of the generated mode.

When magnified, as seen in Figure 4d, the printing steps within the structure were visible and no longer appeared to have a smooth appearance. The printing steps were measured to be approximately 230 nm i.e., the surface roughness lies around 200 nm as is expected for the 63 $\times$  objective lens.

#### 3.2. Optical testing

**Experimental setup.** To test the optics we set up an experiment as seen in Figure 5a. Two sources were used in all experiments: (i) a multiline Ar-ion laser with wavelength selectivity across  $\lambda = 457$  nm, 488 nm, and 514 nm by tuning an internal grating, which could be by-passed for full multi-wavelength operation, and (ii) a Helium–Neon laser to shift the wavelength into the red, at  $\lambda = 633$  nm. In all cases the laser beam was expanded and collimated (when testing optics that rely on complex-amplitude modulation) or imaged (when testing optics that rely on phase-only modulation) using lens  $L_1$  with focal length  $f_1 = 100$  mm, and lens  $L_2$  with focal length  $f_2 = 300$  mm. The beam was then incident on the microscope slide which was composed of an array of 3D printed optical elements. The beam was magnified so that it was large enough to cover the entire area of a single optic, but not so large that it illuminated neighboring optics, as seen in Figure 5 a1. This ensured that the desired mode experienced no interference from modes produced by neighboring optics. Once incident on the hologram, the beam was diffracted into multiple orders, as seen in Figure 5 a2. A lens  $L_3$  with a focal length  $f_3 = 200$  mm was then placed a distance  $f_3$  away and aligned to the +1st-order. Since all the printed optics were designed to have a grating with the same grating frequency, we could maintain the same alignment as we shifted the sample to swap between different optics and thus generated modes.

In the case of testing a printed element with the phase-only modulation, such as a vortex ( $l = 1$ ) mode, the rest of the setup was as follows: close to the Fourier plane a pinhole was placed to select the +1st order with the minimum amount of noise. Ideally the pinhole would be placed in the Fourier plane, but this position was occupied by the charged couple device (CCD) camera. By placing the CCD here, we were able to view the mode in far-field. The intensity image of the beam was then captured.

On the other hand, while testing an element with the complex-amplitude modulation such as a superposition of LG ( $\text{LG}_{l=3}^{p=0} + \text{LG}_{l=-3}^{p=0}$ ) modes, the setup after  $L_3$  was altered. The pinhole was shifted to the Fourier plane located at the focal point of  $L_3$  and an additional lens  $L_4$  with focal length  $f_4 = 200$  mm was then placed a focal length away. The beam was then imaged and viewed using a CCD camera which was placed a distance  $f_4$  away after  $L_4$ . In the image plane, the dispersed broadband beam will be recombined. Therefore, to ensure that the CCD is placed in the correct plane, it was shifted until all the beams appeared as a single mode. Images were taken for each printed element in the sample per discrete wavelength whilst still maintaining the alignment for  $\lambda_0 = 514$  nm.

The quality of the modes created were tested by modal decomposition<sup>[44]</sup> using a digital micro-mirror device (DMD). In

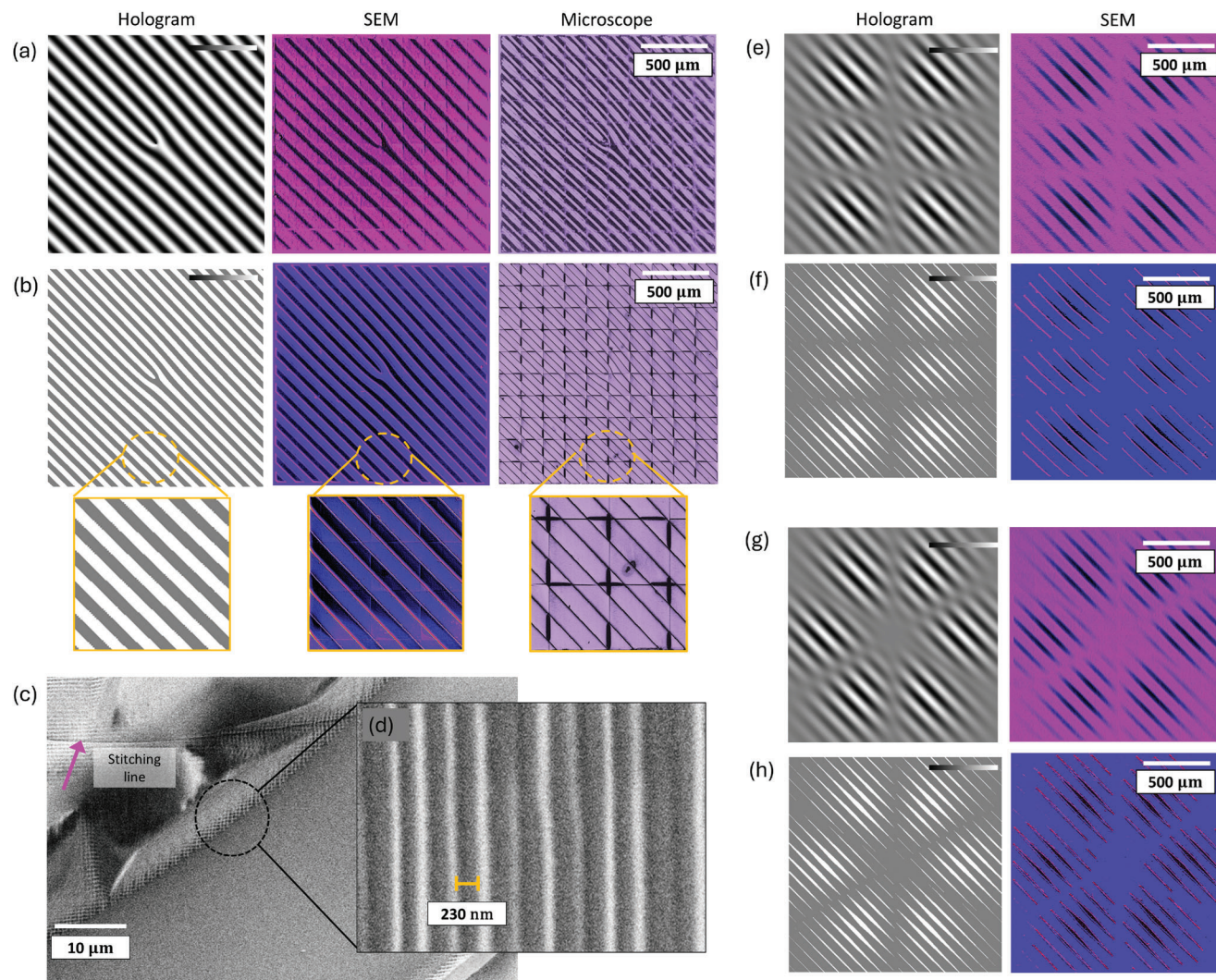


**Figure 4.** Characterization images of printed optics that generate vortex ( $l = 1$ ) through phase-only modulation using a) grayscale with  $\phi \in [-\pi, \pi]$  and b) binary holograms with  $\phi \in [0, \pi]$  (left). Scanning electron microscope (SEM) (middle) and microscopic images (right) are shown of the respective printed optics. A detailed view of the binary hologram and optics are shown (insets (b)) for a region of interest (orange dashed circles). c) Scanning electron microscope (SEM) images depicting the true printing resolution of the Quantum-X Nanoscribe when using a 63 $\times$  objective lens. The discrete printed layers or “steps” are visible and the structure no longer appears continuous. d) When the structure is further magnified (region in marked with a black dashed line in (c)), the distance between these steps, i.e., the surface roughness is measured to be 230 nm. Therefore, the printing resolution of the Quantum-X is approximately 200 nm. The holograms as well as SEM images for the grayscale HG ( $HG_2^1$ ) modes (e), and for the binary ( $HG_2^1$ ) modes (f) are shown. Moreover, (g) shows the grayscale superposition of LG modes ( $LG_3^0 + LG_{-3}^0$ ) and its relevance SEM image. Finally, (h) represents the hologram and SEM images for the binary hologram of LG superposition ( $LG_3^0 + LG_{-3}^0$ ).

the example of the OAM modes, the DMD generated the conjugate of the OAM states under test with the resulting on-axis intensity collected at the Fourier plane of a lens. This provided a quantitative test of modal purity.

**Experimental results.** The experimental results for grayscale optics that generate vortex modes ( $l = 1$  and  $l = 2$ ) through phase-only modulation are shown in Figure 5b as camera images (intensity profiles) for each wavelength, as well as the Multiline (combination of all wavelengths) output. In comparison with the simulated response, we see excellent qualitative agreement, with small distortions likely due to aberrations on the supporting glass slide and the emergence of the expected radial modes due to the

phase-only modulation.<sup>[45,46]</sup> A quantitative analysis is shown in Figure 5c, showing the overlap of each measured mode with the ideal (simulated) beam as a fidelity. The purity at the design wavelength ( $\lambda_0 = 514$  nm) was 100%, while in non-design wavelengths we find purities from 96% to 100%, as given in Table 1. Importantly, the measured purity is has no wavelength trend and can be considered largely independent of wavelength, with the small deviation from ideal due to axial and lateral alignment errors in the modal decomposition set-up when changing wavelength (diffraction is not wavelength independent). A modal decomposition, shown in the inset, reveals the hidden phase structured to confirm the presence of OAM. As seen in the outcome, the OAM

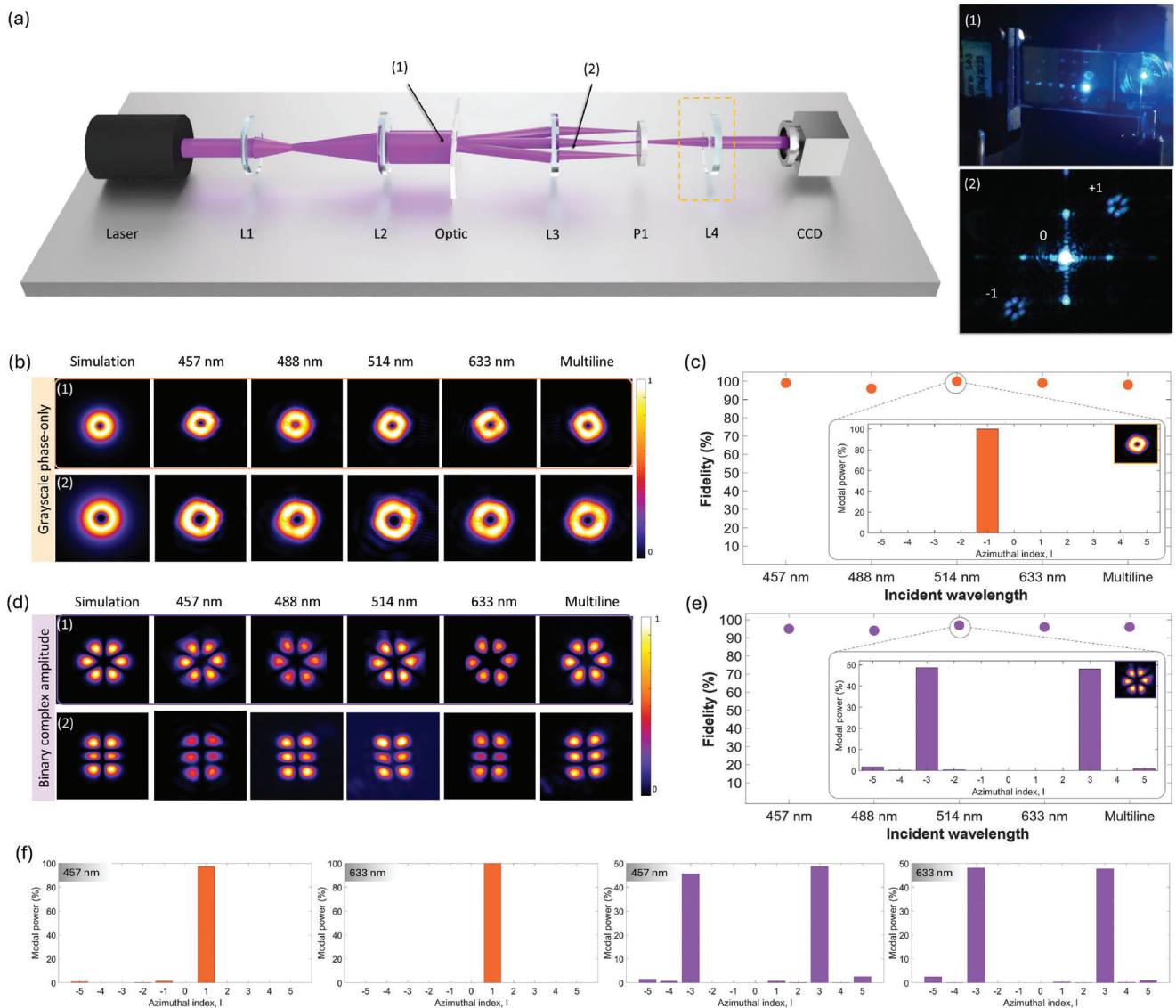


**Figure 5.** Experimental setup and results for optical testing of optics. a) Experimental setup used. The insets (a1), (a2) are an example of the intensity profiles of the beam as seen on a camera at points (1) and (2) in the experimental setup, respectively. b) Transverse intensity profiles of generated modes when various discrete wavelengths (457–633 nm) and a broadband beam (multiline) were incident on an optic designed for  $\lambda_0 = 514$  nm. (b1) vortex ( $l = 1$ ), (b2) vortex ( $l = 2$ ) were generated from optics that were created using grayscale phase-only holograms. c) Fidelity plot for the grayscale phase-only optic that generates vortex ( $l = 1$ ). The (inset) shows the modal decomposition of a mode generated when  $\lambda_0 = 514$  nm was incident on the optic. d) Transverse intensity profiles of generated mode including superposition of  $LG_3^0 + LG_{-3}^0$  (d1) and  $HG_1^2$  (d2) were generated from optics that were created using binary complex-amplitude holograms. e) Fidelity plot for the binary complex-amplitude optic that generates superposition of  $LG_3^0 + LG_{-3}^0$  modes. The (inset) shows the modal decomposition of a mode generated when  $\lambda_0 = 514$  nm was incident on the optic. f) Modal decomposition for non-design wavelengths of 457 and 633 nm, shown for the  $l = 1$  (orange) and  $LG_3^0 + LG_{-3}^0$  (purple) optics.

purity is perfect for the desired mode (shown for  $l = -1$  as an example) with no signal in other modes. These results confirm the expectation of high purity broadband structured light, in this instance, OAM modes as an example. The phase-only design approach ensures good efficiency in the generation process, close to 100% when ignoring small losses due to surface reflections.

Figure 5d shows the experimental results for binary optics based on complex-amplitude modulation, with examples of optics that generate a superposition of LG modes,  $LG_{l=3}^{p=0} + LG_{l=-3}^{p=0}$ ,

shown in the top row, and a pure HG mode of order  $HG_1^2$  as shown in the bottom row. Once again we see excellent qualitative agreement and as mentioned previously with small distortions likely due to aberrations on the supporting glass slide. A quantitative analysis is shown in Figure 5e for the LG superposition example, showing the overlap of each measured mode with the ideal (simulated) beam as a fidelity, confirming the high purity and wavelength independence, with purity results in the 94–97% range. The modal analysis in the inset now shows the

**Table 2.** Printing parameters.

Parameter	Set value
Objective lens	63× NA 1.4
Resin	IP-Dip
Substrate	Microscope slide
Length per optical element (x-direction)	1500 μm
Width per optical element (y-direction)	1500 μm
Height per optical element	25 μm
Hatching distance	0.3 μm
Slicing distance	0.5 μm
Laser power	75 mW
Printing speed	60 mm s <sup>-1</sup>

OAM superposition of  $l = \pm 3$ , each component with nearly equal power, with small cross-talk terms due to the plate aberrations. Finally, Figure 5f shows modal decompositions for two non-design wavelengths (457 nm and 633 nm) as counter examples, using optics designed for  $l = 1$  (orange) and the  $LG_{l=3}^{p=0} + LG_{l=-3}^{p=0}$  superposition (purple). In all cases, we note low cross-talk into unwanted modes and near perfect weighting in the case of the superposition.

We summarise the results in a comparative manner in Table 1. We see that there is only a nominal change in modal purity with wavelength, which we attribute to the small alignment errors when altering the set-up from the design to the non-design wavelengths. These arise due to diffraction effects, e.g., the grating term in the hologram moving the fields laterally and small axial size changes with propagation, both of which have small contributions to the modal analysis. Nevertheless, these results represent excellent performance when compared to alternative approaches reported in the literature. Modal purities can be designed to be very high, for instance, by metasurfaces with amplitude and phase control,<sup>[47,48]</sup> cascading phase-only metasurfaces<sup>[49]</sup> or by employing laser cavities with metasurfaces,<sup>[50]</sup> but these purities are reported from single wavelength systems of complex design. As far as we are aware, our study is the first to report multi-wavelength purities, and comes with the benefit of a simple design and implementation approach. Although there is no theoretical limit to the modal purities our approach can attain (in principle 100%), practical issues such as optical aberrations will always result in slightly lower values.

## 4. Discussion and Conclusion

We have shown how to design and fabricate customized optics for broadband structured, marrying tools from Fourier optics and modern 3D laser direct writing based on two-photon polymerization. To fabricate the desired optical design, the laser power was used to control the voxel to produce grayscale structures covering phase-only and complex amplitude transmission functions. Optical testing of these mini-optical structures confirmed the predicted high modal purities and wavelength independence. This demonstration of compact and affordable solutions for broadband structured light opens a path to a myriad of

implementations. These include fundamental control of light's degrees of freedom beyond the traditional for multi-modal light control,<sup>[51]</sup> revealing novel forms of light in the spatio-temporal domain.<sup>[52]</sup> Such control opens new applications that exploits multi-wavelength structured light, for instance higher data rates in encryption<sup>[34,53]</sup> and communication<sup>[54]</sup> by using both spatial and wavelength as encoding alphabets, simulating quantum processing based on space and spectral non-separability,<sup>[55]</sup> as well as imaging and sensing in spectral and spatial domains simultaneously.<sup>[56,57]</sup>

## 5. Experimental Section

**Calibration:** To calibrate the system, a prescribed printing design was uploaded to the instrument composed of a  $3 \times 3$  array of convex lenses in the form of a 16-bit grayscale image. The array was set as 40 μm lens diameters with a spacing of 15 μm between each element. Size of each lens was set so that the entire array was within the field of view of the objective lens. Here the calibration was performed using a 63× objective lens, so each lens was set to a size of 40 μm with a spacing of 15 μm between. A summary of the printing parameters and their chosen set values are given in Table 2. These operation parameters were set as given by the manufacturer based on a good compromise between quality and printing speed, and used in calibration and final production. The design was then printed and developed using the typical fabrication process as mentioned in Section 3. One sample of each type was metallized with a thin layer ( $\approx 3\text{--}5$  nm) of silver by sputtering, for subsequent characterization steps by 3D Scanning microscope (Olympus LEXT) and Scanning Electron Microscope (SEM) to recover a height map of the printed structure. The file was then uploaded to the GrayScribeX software which converted it into a grayscale image and compared this to the pre-loaded design lens-by-lens. A plot of the printed height versus the applied laser power per lens was created and the average of all the plotted curves then was served as the final calibration curve.

## Acknowledgements

The Microscopy and Microanalysis Unit at the University of the Witwatersrand for the scanning electron microscope (SEM) images and additional characterization of the printed optics. J.G.K. and S.H. acknowledge support from the Deutsche Forschungsgemeinschaft (DFG, German Research Foundation) under Germany's Excellence Strategy via the Excellence Cluster 3D Matter Made to Order (EXC-2082/1–390761711), and the European Research Council (ERC) Synergy grant SygG 951459 HiSCORE, which funded the Nanoscribe Quantum-X.

## Conflict of Interest

The authors declare no conflict of interest.

## Data Availability Statement

The data that support the findings of this study are available from the corresponding author upon reasonable request.

## Keywords

3D printed optics, broadband beam shaping, diffractive optical elements, optical angular momentum, structured light

Received: November 6, 2024  
Revised: January 10, 2025  
Published online:

- [1] A. Forbes, M. De Oliveira, M. R. Dennis, *Nat. Photonics* **2021**, *15*, 253.
- [2] C. He, Y. Shen, A. Forbes, *Light: Sci. Appl.* **2022**, *11*, 205.
- [3] K. Y. Bliokh, E. Karimi, M. J. Padgett, M. A. Alonso, M. R. Dennis, A. Dudley, A. Forbes, S. Zahedpour, S. W. Hancock, H. M. Milchberg, S. Rotter, F. Nori, S. K. Özdemir, N. Bender, H. Cao, P. B. Corkum, C. Hernández-García, H. Ren, Y. Kivshar, M. G. Silveirinha, Nader Engheta, A. Rauschenbeutel, P. Schneeweiss, J. Volz, D. Leykam, D. A. Smirnova, K. Rong, B. Wang, E. Hasman, M. F. Picardi, A. V. Zayats, et al., *J. Opt.* **2023**, *25*, 103001.
- [4] J. Harrison, D. Naidoo, A. Forbes, A. Dudley, *Adv. Phys.: X* **2024**, *9*, 2327453.
- [5] I. Nape, B. Sephton, P. Ornelas, C. Moodley, A. Forbes, *APL Photonics* **2023**, *8*, 5.
- [6] W. T. Buono, A. Forbes, *Opto-Electronic Advances* **2022**, *5*, 210174.
- [7] A. Forbes, *Laser Photonics Rev.* **2019**, *13*, 1900140.
- [8] Y. Shen, Q. Zhan, L. G. Wright, D. N. Christodoulides, F. W. Wise, A. E. Willner, K.-h. Zou, Z. Zhao, M. A. Porras, A. Chong, C. Wan, K. Y. Bliokh, C.-T. Liao, C. Hernández-García, M. Murnane, M. Yessenov, A. F. Abouraddy, L. J. Wong, M. Go, S. Kumar, C. Guo, S. Fan, N. Papisimakis, N. I. Zheludev, L. Chen, W. Zhu, A. Agrawal, M. Mounaix, N. K. Fontaine, J. Carpenter, et al., *J. Opt.* **2023**, *25*, 093001.
- [9] N. M. Litchinitser, *Science* **2012**, *337*, 1054.
- [10] X. Luo, M. Pu, F. Zhang, M. Xu, Y. Guo, X. Li, X. Ma, *J. Appl. Physcol.* **2022**, *131*, 18.
- [11] L. Zhou, T. Zhong, Y. Liu, T. Yu, K. Neyts, Z. Luo, H. Wang, J. Sun, J. Zhou, Y. Shen, *Adv. Funct. Mater.* **2024**, 2404614.
- [12] T. Omatsu, K. Miyamoto, K. Toyoda, R. Morita, Y. Arita, K. Dholakia, *Adv. Opt. Mater.* **2019**, *7*, 1801672.
- [13] N. Yu, P. Genevet, M. A. Kats, F. Aieta, J.-P. Tetienne, F. Capasso, Z. Gaburro, *Science* **2011**, *334*, 333.
- [14] Y. Yang, Y.-X. Ren, M. Chen, Y. Arita, C. Rosales-Guzmán, *Adv. Photon.* **2021**, *3*, 034001.
- [15] A. H. Dorrah, F. Capasso, *Science* **2022**, *376*, eabi6860.
- [16] P. Genevet, F. Capasso, *Rep. Prog. Phys.* **2015**, *78*, 024401.
- [17] A. I. Kuznetsov, M. L. Brongersma, J. Yao, M. K. Chen, U. Levy, D. P. Tsai, N. I. Zheludev, A. Faraon, A. Arbabi, N. Yu, D. Chanda, K. B. Crozier, A. Alù, *ACS photonics* **2024**, *11*, 816.
- [18] S. A. Schulz, R. Oulton, M. Kenney, A. Alù, I. Staude, A. Bashiri, Z. Fedorova, R. Kolkowski, A. F. Koenderink, X. Xiao, J. Yang, W. J. Peveler, A. W. Clark, G. Perrakis, A. C. Tasolamprou, M. Kafesaki, A. Zaleska, W. Dickson, D. Richards, A. Z. Ren, Y. Kivshar, S. Maier, X. Chen, M. A. Ansari, Y. Gan, A. Alexeev, T. F. Krauss, A. Di Falco, S. D. Gennaro, T. Santiago-Cruz, et al., *Appl. Phys. Lett.* **2024**, *124*, 26.
- [19] X. Luo, *ACS Photonics* **2023**, *10*, 2116.
- [20] Y. Yang, A. Forbes, L. Cao, *Opto-Electron. Sci.* **2023**, *2*, 230026.
- [21] S. Scholes, R. Kara, J. Pinnell, V. Rodríguez-Fajardo, A. Forbes, *Opt. Eng.* **2020**, *59*, 041202.
- [22] X.-B. Hu, C. Rosales-Guzmán, *J. Opt.* **2022**, *24*, 034001.
- [23] W. T. Chen, A. Y. Zhu, F. Capasso, *Nat. Rev. Mater.* **2020**, *5*, 604.
- [24] W. T. Chen, A. Y. Zhu, V. Sanjeev, M. Khorasaninejad, Z. Shi, E. Lee, F. Capasso, *Nat. Nanotechnol.* **2018**, *13*, 220.
- [25] S. Wang, P. C. Wu, V.-C. Su, Y.-C. Lai, M.-K. Chen, H. Y. Kuo, B. H. Chen, Y. H. Chen, T.-T. Huang, J.-H. Wang, R. M. Lin, C. H. Kuan, T. Li, Z. Wang, S. Zhu, D. P. Tsai, *Nat. Nanotechnol.* **2018**, *13*, 227.
- [26] S. Wang, P. C. Wu, V.-C. Su, Y.-C. Lai, C. Hung Chu, J.-W. Chen, S.-H. Lu, J. Chen, B. Xu, C.-H. Kuan, T. Li, S. Zhu, D. P. Tsai, *Nat. Commun.* **2017**, *8*, 187.
- [27] H. Ren, J. Jang, C. Li, A. Aigner, M. Plidschun, J. Kim, J. Rho, M. A. Schmidt, S. A. Maier, *Nat. Commun.* **2022**, *13*, 4183.
- [28] Y. Liu, L. Zhou, M. Guo, Z. Xu, J. Ma, Y. Wen, N. M. Litchinitser, Y. Shen, J. Sun, J. Zhou, *Adv. Mater.* **2024**, 2412007.
- [29] Y. Liu, L. Zhou, Y. Wen, Y. Shen, J. Sun, J. Zhou, *Nano Lett.* **2022**, *22*, 2444.
- [30] M. Pu, X. Li, X. Ma, Y. Wang, Z. Zhao, C. Wang, C. Hu, P. Gao, C. Huang, H. Ren, X. Li, F. Qin, J. Yang, M. Gu, M. Hong, X. Luo, *Sci. Adv.* **2015**, *1*, e1500396.
- [31] Z. Shi, M. Khorasaninejad, Y.-W. Huang, C. Roques-Carmes, A. Y. Zhu, W. T. Chen, V. Sanjeev, Z.-W. Ding, M. Tamagnone, K. Chaudhary, R. C. Devlin, C.-W. Qiu, F. Capasso, *Nano Lett.* **2018**, *18*, 2420.
- [32] V. V. Kotlyar, A. A. Kovalev, A. G. Nalimov, S. S. Staifeev, In *Photonics*, Vol. 9, MDPI, **2022**, p. 145.
- [33] Y. Aslani, A. Toulouse, M. Schmid, H. Giessen, T. Haist, A. Herkommer, *Opt. Mater. Express* **2023**, *13*, 1372.
- [34] H. Wang, H. Wang, Q. Ruan, J. Y. E. Chan, W. Zhang, H. Liu, S. D. Rezaei, J. Trisno, C.-W. Qiu, M. Gu, J. K. W. Yang, *Nat. Nanotechnol.* **2023**, *18*, 264.
- [35] A. Forbes, L. Perumal, *Nat. Nanotechnol.* **2023**, *18*, 221.
- [36] V. Arrizón, U. Ruiz, R. Carrada, L. A. González, *JOSA A* **2007**, *24*, 3500.
- [37] A. Forbes, L. Mkhumbuzza, L. Feng, *Nat. Rev. Phys.* **2024**, *1*.
- [38] D.-M. Spangenberg, A. Dudley, P. H. Neethling, E. G. Rohwer, A. Forbes, *Opt. Express* **2014**, *22*, 13870.
- [39] Christopher Stilson, R. Pal, R. A. C. Jr, *Proc. SPIE Micromachining and Microfabrication Process Technology* **2014**, *XIX*, 89730E.
- [40] W. Kaiser, C. G. B. Garrett, *Phys. Rev. Lett.* **1961**, *7*, 229.
- [41] S. Maruo, O. Nakamura, S. Kawata, *Opt. Lett.* **1997**, *22*, 132.
- [42] J. F. Gottwald, *United States Patent*, 3,596,285.
- [43] M. Emons, K. Obata, T. Binhammer, A. Ovsianikov, B. N. Chichkov, U. Morgner, *Opt. Mater. Express* **2012**, *2*, 942.
- [44] J. Pinnell, I. Nape, B. Sephton, M. A. Cox, V. Rodríguez-Fajardo, A. Forbes, *JOSA A* **2020**, *37*, C146.
- [45] B. Sephton, A. Dudley, A. Forbes, *Appl. Opt.* **2016**, *55*, 7830.
- [46] I. Nape, B. Sephton, Y.-W. Huang, A. Vallés, C.-W. Qiu, A. Ambrosio, F. Capasso, A. Forbes, *APL Photonics* **2020**, *5*, 7.
- [47] S. Zheng, H. Hao, Y. Tang, X. Ran, *Opt. Lett.* **2021**, *46*, 5790.
- [48] M. de Oliveira, M. Piccardo, S. Eslami, V. Aglieri, A. Toma, A. Ambrosio, *ACS photonics* **2023**, *10*, 290.
- [49] F. Mei, G. Qu, X. Sha, J. Han, M. Yu, H. Li, Q. Chen, Z. Ji, J. Ni, C.-W. Qiu, et al., *Nat. Commun.* **2023**, *14*, 6410.
- [50] H. Sroor, Y.-W. Huang, B. Sephton, D. Naidoo, A. Vallés, V. Ginis, C.-W. Qiu, A. Ambrosio, F. Capasso, A. Forbes, *Nat. Photonics* **2020**, *14*, 498.
- [51] M. Piccardo, V. Ginis, A. Forbes, S. Mahler, A. A. Friesem, N. Davidson, H. Ren, A. H. Dorrah, F. Capasso, F. T. Dullo, et al., *J. Opt.* **2021**, *24*, 013001.
- [52] C. Wan, A. Chong, Q. Zhan, *eLight* **2023**, *3*, 11.
- [53] X. Fang, H. Ren, M. Gu, *Nat. Photonics* **2020**, *14*, 102.
- [54] X. Wang, C. Wang, M. Cheng, B. Yang, Z. Xie, Y. He, J. Xiao, H. Ye, Y. Li, D. Fan, et al., *J. Lightwave Technol.* **2021**, *39*, 2830.
- [55] L. Kopf, R. Barros, R. Fickler, *ACS Photonics* **2023**, *11*, 241.
- [56] S. Goossens, G. Navickaitė, C. Monasterio, S. Gupta, J. J. Piqueras, R. Pérez, G. Burwell, I. Nikitskiy, T. Lasanta, T. Galán, et al., *Nat. Photonics* **2017**, *11*, 366.
- [57] L. Bian, Z. Wang, Y. Zhang, L. Li, Y. Zhang, C. Yang, W. Fang, J. Zhao, C. Zhu, Q. Meng, et al., *Nature* **2024**, *635*, 73.